Double-Exchange Interaction in Optically Induced Nonequilibrium State: A Conversion from Ferromagnetic to Antiferromagnetic Structure

Atsushi Ono and Sumio Ishihara
Department of Physics, Tohoku University, Sendai 980-8578, Japan

(Received 29 April 2017; revised manuscript received 19 September 2017; published 16 November 2017)

The double-exchange (DE) interaction, that is, a ferromagnetic (FM) interaction due to a combination of electron motion and the Hund coupling, is a well-known source of a wide class of FM orders. Here, we show that the DE interaction in highly photoexcited states is antiferromagnetic (AFM). Transient dynamics of quantum electrons coupled with classical spins are analyzed. An ac field applied to a metallic FM state results in an almost perfect Néel state. A time characterizing the FM-to-AFM conversion is scaled by light amplitude and frequency. This hidden AFM interaction is attributable to the electron-spin coupling under nonequilibrium electron distribution.

DOI: 10.1103/PhysRevLett.119.207202

Ultrafast optical manipulation of magnetism is widely accepted as a fascinating research topic in modern condensed matter physics [1–3] from the viewpoints of fundamental physics and technological applications owing to the recent significant progress in optical laser techniques. Beyond the ultrafast demagnetization due to a rapid spin-temperature increase [4], various controls of magnetism, often utilizing photoinduced magnetic phase transition, have been demonstrated as promising strategies in subpicosecond time scales [1,5–7]. The most efficient and direct method is by adjusting the magnetic exchange interactions acting on electron spins by light [8,9]. This subject in highly nonequilibrium states essentially concerns the microscopic nature of electrons, e.g., the band structure, electron correlation, and relaxation processes.

Among a number of exchange couplings, the double-exchange (DE) interaction is widely recognized as a representative microscopic source of the ferromagnetic (FM) phenomena. The DE interaction was originally proposed by Zener and Anderson-Hasegawa for FM oxides [10–12]. Elemental constituents of the DE interaction are mobile electrons and electron spins localized at lattice sites. The intra-atomic FM interaction, that is, the Hund coupling (J_H), connects these two constituents. When the Hund coupling is sufficiently larger than the electron hopping (t) for the mobile electrons, the spins align ferromagnetically [see Fig. 1(a)], and thus electronic transport strongly correlates with magnetism. This correlation in the DE interaction has been observed ubiquitously in a wide variety of magnets and magnetic phenomena, such as colossal magnetoresistance [13], f-electron ferromagnetism [14], molecular magnets [15], anomalous Hall effect [16], Skyrmion physics [17], and spintronics devices [18].

This electron-spin coupling also provides a promising route to the ultrafast optical manipulation of magnetism owing to the direct connection between the electrons and light. A number of the photoinduced magnetization changes have been confirmed experimentally [19–25] and theoretically [26–31] in magnets, in which the DE interaction works in equilibrium states. In most cases, the laser light is applied into a narrow-band insulating phase associated with the antiferromagnetic (AFM) order, which is realized through the interactions additional to the original DE system. The experimentally observed formations of a metallic FM state are explained well within a naive extension of the DE interaction to the photoexcited states [28,29]; kinetic motions of photogenerated carriers align spins ferromagnetically associated with an increase of the electronic bandwidth.

In this Letter, in contrast to a naive extension of the DE interaction picture, we show that the DE interaction in highly optically excited states is AFM [see Fig. 1(b)]. We analyze the minimal model for the DE interaction, consisting of classical spins and quantum electrons, in which no explicit AFM interactions are included. Coupled time-dependent equations are solved numerically in finite-size

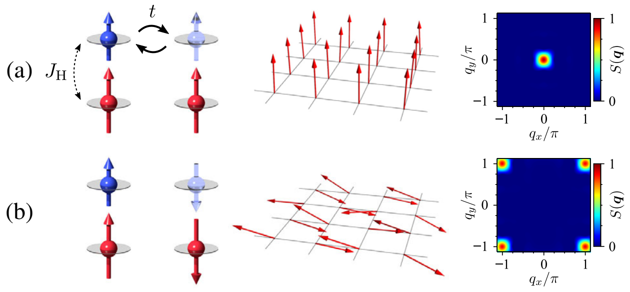

FIG. 1. Illustrations of the DE interaction, calculated spin configurations, and calculated intensity maps of the spin structure factors in the momentum space in (a) the equilibrium FM state, and (b) the transient photoexcited AFM state. Long and short bold arrows at left represent localized spins and mobile electrons, respectively. Two-dimensional square lattice is adopted in the calculations.

clusters. We introduce the continuous wave (cw) field, in which the frequency is chosen to induce the intraband electronic excitations. It is found that an initial metallic FM state is converted to an AFM state. A time scale characterizing the FM-to-AFM conversion is controlled by light amplitude and frequency, as well as spin damping. Several types of effective and realistic photoexcitations are proposed. The photoinduced AFM state is well demonstrated using a tight-binding model with a nonequilibrium electron distribution. Possible observation methods are proposed.

The DE model we analyze describes the itinerant electrons coupled with the localized spins. This is defined as

$$\mathcal{H} = -\sum_{\langle ij\rangle s} t_{ij} c_{is}^{\dagger} c_{js} - J_H \sum_{iss'} \boldsymbol{S}_i \cdot c_{is}^{\dagger} \boldsymbol{\sigma}_{ss'} c_{is'}, \qquad (1)$$

where $c_{is}^{\dagger}$ (c_{is}) is the creation (annihilation) operator for an electron at site i with spin $s(=\uparrow,\downarrow)$, $\boldsymbol{\sigma}$ are the Pauli matrices, and $\boldsymbol{S}_i$ is a localized spin operator with magnitude S. The first term ($\mathcal{H}_t$) represents the electron hopping between the nearest-neighbor sites with the hopping integral t_{ij}, and the second term ($\mathcal{H}_H$) represents the Hund coupling with $J_H(>0)$. The total numbers of sites and electrons, and the electron density are represented by N_L, N_e, and $n \equiv N_e/N_L$, respectively. The time-dependent vector potential $\boldsymbol{A}(\tau)$ is introduced as the Peierls phase as $t_{ij} \to t e^{-i\boldsymbol{A}(\tau)\cdot(\boldsymbol{r}_i - \boldsymbol{r}_j)}$ with the position vector $\boldsymbol{r}_i$ of site i. The lattice constant, elementary charge, and Planck constant are set to 1, and the Coulomb gauge is adopted. The Hamiltonian in Eq. (1) without $\boldsymbol{A}(\tau)$ in equilibrium has been studied well so far [32], and the FM metallic state is realized in a wide parameter range around $n = 0.5$ and large $J_H/t(\gtrsim 2)$. No AFM interactions are included explicitly [33].

The ground and transient states are examined numerically in finite-size clusters [29,34], in which $\boldsymbol{S}_i$ are treated as classical spins, justified in the limit of large S. The electron operators $\psi_\nu(\tau)$ and energies $\varepsilon_\nu(\tau)$ are obtained by diagonalizing the Hamiltonian, and the electronic wave function is calculated as $|\Psi(\tau)\rangle = \prod_{\nu=1}^{N_e} \psi_\nu^{\dagger}(\tau)|0\rangle$ with the vacuum $|0\rangle$. The field operators at $\tau + \delta\tau$ with small time interval $\delta\tau$ is generated as $\psi_\nu^{\dagger}(\tau+\delta\tau) = e^{i\mathcal{H}(\tau)\delta\tau} \psi_\nu^{\dagger}(\tau) e^{-i\mathcal{H}(\tau)\delta\tau}$. Dynamics of the classical spins are calculated using the Landau-Lifshitz-Gilbert equation, $\dot{\boldsymbol{S}}_i = \boldsymbol{h}_i^{\mathrm{eff}} \times \boldsymbol{S}_i + \alpha \boldsymbol{S}_i \times \dot{\boldsymbol{S}}_i$, where $\boldsymbol{h}_i^{\mathrm{eff}}(\tau) = -\langle \Psi(\tau)|\partial\mathcal{H}/\partial\boldsymbol{S}_i|\Psi(\tau)\rangle$ and α are an effective field and a damping constant, respectively. The two-dimensional square lattice of $N_L = L^2$ sites ($L \leq 16$) with the periodic (antiperiodic) boundary condition along the x (y) direction are adopted. The cluster sizes are sufficient to obtain the results with high reliability as shown in the Supplemental Material [34]. A small randomness is introduced in $\boldsymbol{S}_i$ at each site in the initial state, in which the maximum deviation in the polar angle is $\delta\theta = 0.1$ corresponding to thermal fluctuation at temperature of approximately $0.001t$ [29,34]. For most of the numerical calculations, we utilize $L = 8$, $n = 0.5$, $SJ_H/t = 4$, and $S\alpha = 1$. We confirmed that the characteristic results shown below are observed in a wide parameter range. For a typical value of $t = 0.5$ eV in the manganese oxides, a time unit of $\tau = 1/t$ is approximately 8 fs.

First, we introduce the transient dynamics induced by the cw light represented by $\boldsymbol{A}(\tau) = (\boldsymbol{A}_0/\omega)\theta(\tau)\sin(\omega\tau)$ with frequency ω and amplitude A_0 [35]. We chose $\omega/t = 1$ and $\boldsymbol{A}_0 = A_0(\hat{x}+\hat{y})$, where $\hat{x}$ ($\hat{y}$) is a unit vector along x (y). The detailed A_0/ω dependence is shown later. The time profiles of the energies, electronic bands, and spin structure factors $S(\boldsymbol{q}) = N_L^{-2}\sum_{i,j} e^{i\boldsymbol{q}\cdot(\boldsymbol{r}_i-\boldsymbol{r}_j)} \boldsymbol{S}_i \cdot \boldsymbol{S}_j$ are presented in Figs. 2(a), 2(b), and 2(c), respectively. Figure 2(c) displays the main result; the dominant spin structure is interchanged from FM to AFM states, in which $S(\pi,\pi)$ is approximately 90% of its maximum value. Intensity maps of $S(\boldsymbol{q})$ at $\tau t = 0$, 50, 70, and 300 are shown in Figs. 1(a), 2(d), 2(e), and 1(b), respectively. An animation of the real-space spin dynamics is presented in the Supplemental Material [34]. This FM-to-AFM conversion is clearly in contrast to the photodoping effect in the DE model, in which the enhancement of the FM interaction is expected [19,27,29].

The photoinduced dynamics shown in Figs. 2(a)–2(c) is summarized as follows. (i) ($\tau < 0$): Before photoirradiation, the metallic FM state is realized because of the DE interaction [see Fig. 1(a)]. The lower and upper bands are identified as the major- and minor-spin bands, respectively. The separations between the band centers and each band width (W) are $2SJ_H$ and $8t$, respectively. The Fermi level is located at the middle of the lower band, indicating a half-metallic ferromagnet [36]. (ii) ($0 \lesssim \tau t \lesssim 30$): After turning

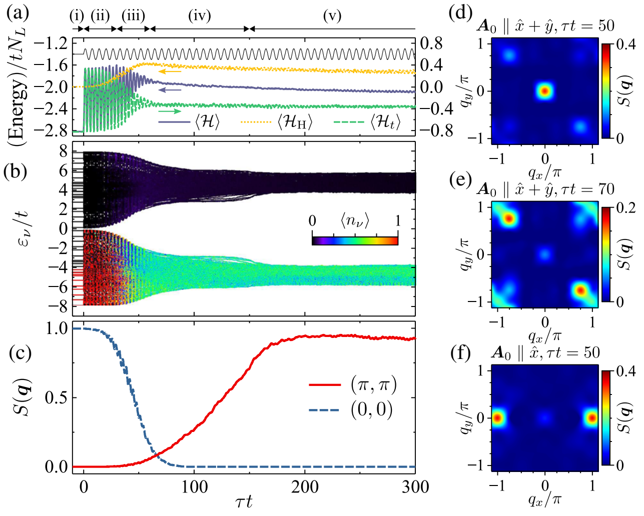

FIG. 2. Time profiles of the electronic and spin structures induced by the cw light, where $\boldsymbol{A}_0$ is parallel to $\hat{x}+\hat{y}$. (a) $\boldsymbol{A}(\tau)$, $\langle\mathcal{H}\rangle$, $\langle\mathcal{H}_t\rangle$, and $\langle\mathcal{H}_H\rangle$, (b) energy levels ($\varepsilon_\nu$), and electron population ($\langle n_\nu\rangle$), and (c) $S(0,0)$ and $S(\pi,\pi)$. (d)–(f) Intensity maps of $S(\boldsymbol{q})$. We chose $\tau t = 50$ and $\boldsymbol{A}_0\|\hat{x}+\hat{y}$ in (d), $\tau t = 70$ and $\boldsymbol{A}_0\|\hat{x}+\hat{y}$ in (e), and $\tau t = 50$ and $\boldsymbol{A}_0\|\hat{x}$ in (f). Other parameter values are $A_0/t = 2$ and $\omega/t = 1$.

on the cw field, $\langle \mathcal{H}_t \rangle$ starts oscillating with a frequency of 2ω. The electrons are excited inside the lower band, and the occupied ($\langle n_\nu \rangle \sim 1$) and unoccupied ($\langle n_\nu \rangle \sim 0$) levels are intermingled inside the lower band. Changes in the electronic state at an early stage are explained through the dynamical localization (DL) phenomenon, as shown later. (iii) ($30 \lesssim \tau t \lesssim 60$): Abrupt reductions of W and $S(0,0)$ occur cooperatively, which promote the changes in the electron distribution inside the lower band further. The electrons distribute almost uniformly in the lower band with $\langle n_\nu \rangle \sim 0.5$. The upper band is almost empty, implying that the injected energy is much lower than the upper bound of the energy spectrum. The time when $S(0,0)$ steeply decreases is termed τ_F. The transient spin structure depends on the polarization of light [see Fig. 2(f) for $\boldsymbol{A}_0 = \sqrt{2} A_0 \hat{x}$]. (iv) ($60 \lesssim \tau t \lesssim 150$): $S(\pi,\pi)$ appears and increases; The time when $S(\pi,\pi)$ steeply increases is termed τ_{AF}. A time lag between τ_F and τ_{AF} is explained further later. (v) ($150 \lesssim \tau t$): An AFM steady state is realized, and the gap between the two bands is approximately $2SJ_H$. The spin structure and the intensity map of $S(\boldsymbol{q})$ are shown in Fig. 1(b).

Next, we show the key factors that control the times characterizing the FM-to-AFM conversion. As shown in the detailed α dependence presented in the Supplemental Material, the time scales for the FM-to-AFM conversion increase with decreasing α, as expected. Here, we show that A_0 and ω are the additional key parameters controlling the conversion times. The time profiles of W, electron number in the upper band (N_e^{upper}), $S(0,0)$, and $S(\pi,\pi)$ are presented for several values of A_0 in Figs. 3(a)–3(d) at fixed ω. The decrease in $S(0,0)$ is promoted with increasing A_0. A steplike feature appears in the time profiles in W at $W \sim 3$. The time when W decreases steeply and that around the edge of the steplike feature correspond to τ_F and τ_{AF}, respectively [see bold arrows in Figs. 3(a), 3(c), and 3(d) for $A_0/t = 1.55$]. At around τ_F, electrons are excited from the lower to upper bands by the excess energy due to the FM order destruction, as indicated in Fig. 3(b). Then, the electrons relax to the lower band associated with development of $S(\pi,\pi)$ at around τ_{AF}. The electron excitation and relaxation between the lower and upper bands are attributed to the Hund coupling. Because of these intricate interband excitation and relaxation processes, τ_{AF} does not show monotonic dependence on A_0. On the other hand, τ_F is well scaled by A_0/ω, as shown in Fig. 3(e); data sets can be fitted by function $(A_0/\omega - c)^\gamma$ with numerical constants $c(\sim 1.1–1.3)$ and $\gamma(\sim -1)$. A finite c implies that the threshold values of A_0/ω exist for the FM-to-AFM conversion.

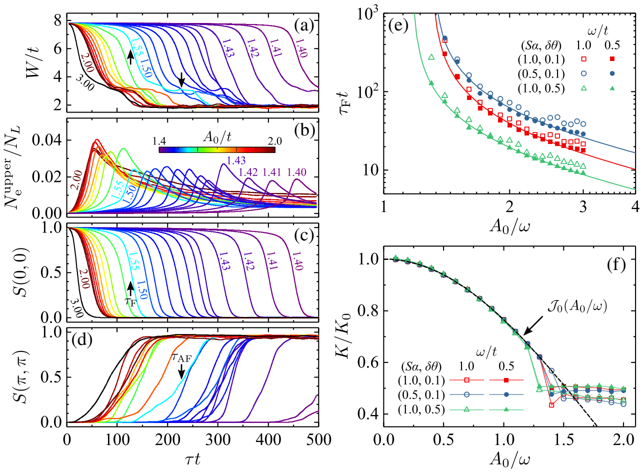

FIG. 3. (a)–(d) Time profiles of the bandwidth, electron number density in the upper band, $S(0,0)$, and $S(\pi,\pi)$ induced by cw lights for several values of A_0. We chose $\omega/t = 1$. (e) τ_F plotted as functions of A_0/ω for several sets of $(S\alpha, \delta\theta)$. The bold lines represent the function $(A_0/\omega - c)^\gamma$. (f) The normalized kinetic energy (K/K_0) averaged between $\tau t = 400$–500 (see text) plotted as functions of A_0/ω. The bold line represents the zeroth-order Bessel function $\mathcal{J}_0(A_0/\omega)$.

Here, we briefly point out that the transient dynamics just after turning on the cw light are understood in the generalized DL phenomenon, which was originally proposed in the noninteracting system under the cw field [37–39]. The averaged kinetic energy in the early part of the time domain (ii) is plotted as functions of A_0/ω in Fig. 3(f) [40]. We define $K \equiv (\Delta T)^{-1} \int_{\Delta T} d\tau \langle \mathcal{H}_t \rangle$ with the time interval ΔT and the kinetic energy before irradiation K_0. The calculated data sets are scaled by a universal curve, and can be fitted by the zeroth-order Bessel function $\mathcal{J}_0(A_0/\omega)$ predicted by the DL theory. Deviation of the numerical data from $\mathcal{J}_0(A_0/\omega)$ is seen in $A_0/\omega \gtrsim 1.25$. This is attributable to the spin structure change which is beyond the DL scope. After the early part of the time domain (ii), corresponding to $\tau \gtrsim 10/t$ in Fig. 2(b), fitting of the numerical data by $\mathcal{J}_0(A_0/\omega)$ does not work, because the spin structure starts changing.

The photoinduced FM-to-AFM conversion occurs not only by the cw light, but also by various realistic methods of light irradiation. Instead of the cw field, we introduce a sudden quench of the vector potential simply modeled as $\boldsymbol{A}(\tau) = \boldsymbol{A}_1 \theta(\tau)$, which is equivalent to the electric field pulse $\boldsymbol{E}(\tau) = -\boldsymbol{A}_1 \delta(\tau)$. This asymmetric pulse causes a nonadiabatic momentum shift of electrons by $\delta\boldsymbol{k} = \int d\tau \boldsymbol{E}(\tau)$, which induces the population inversion [41]. The population inversions induced by light have been studied in a variety of interacting electron systems [42–44]. The time profiles of the electronic energy bands, electron population, and $S(\boldsymbol{q})$ are presented in Figs. 4(a) and 4(c), in which we chose $\delta\boldsymbol{k} = (\pi,\pi)$ [35]. Immediately after pulse irradiation, the population inversion is realized inside the lower band as expected, and W and $S(0,0)$ are reduced. Then, the electrons distribute almost uniformly in the narrow lower band, and $S(\pi,\pi)$ emerges at $\tau t \sim 50$. Finally, the metallic FM state is recovered, and the electrons thermalize. Another type of effective light irradiation is a combination of a pulse field and a delayed cw field modeled as

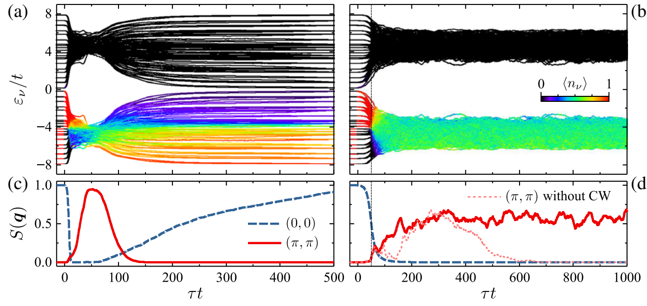

FIG. 4. Time profiles of the energy levels (ε_ν), electron distributions ($\langle n_\nu \rangle$), $S(0,0)$, and $S(\pi,\pi)$ with (a),(c) the pulse electric field and (b),(d) the combination of pulse and cw fields (see text). A dotted line in (d) represents $S(\pi,\pi)$ without $\boldsymbol{A}_1$. Here, $\boldsymbol{A}_1 = \pi(\hat{x}+\hat{y})$ and $S\alpha = 1$ in (a),(c); $\boldsymbol{A}_1 = \pi(\hat{x}+\hat{y})$, $\boldsymbol{A}_0/t = 0.3(\hat{x}+\hat{y})$, $\tau_0 t = 50$, and $S\alpha = 0.1$ in (b),(d); and $\omega/t = 1$ in (a)–(d).

$$\boldsymbol{E}(\tau) = -\partial_\tau \boldsymbol{A}(\tau) = -\boldsymbol{A}_1\delta(\tau) - \boldsymbol{A}_0 \cos[\omega(\tau-\tau_0)]\theta(\tau-\tau_0)$$

with delay time τ_0. As shown in Figs. 4(b) and 4(d), the pulse field generates population inversion inside the lower band, and the subsequent cw field maintains the AFM state. In contrast, in the case without the subsequent cw field ($A_0 = 0$), $S(\pi,\pi)$ disappears gradually [a dotted line in Fig. 4(d)]. An advantage in this pulse-cw combination is that a 1 order weaker A_0 is required to maintain the AFM state than the A_0 value in the case where the cw field is only introduced (see Fig. 2). The spin conversion by use of the pulse field might be more realistic rather than the cw light.

Now, we focus on the photoinduced AFM steady state. Instead of a rigorous analysis of this nonequilibrium state in the open many-body system, which is beyond the scope of the present work, we evaluate the energies in the idealized FM and AFM states under a hypothetic electron distribution. The transient electronic density of states (DOS) and the electron population in the FM state ($\tau = 0$) and photoinduced AFM state ($\tau = 300/t$) are shown in Figs. 5(a) and 5(b), respectively, in which the cw field is applied. In contrast to the equilibrium FM state, where the electrons occupy from the bottom to the Fermi level, the electrons in the AFM state distribute almost uniformly, as suggested previously. Thus, we introduce the idealized FM and AFM orders in Eq. (1), and the uniform electron distribution in the lower band, that is, $\langle n_\nu \rangle = n$ ($\langle n_\nu \rangle = 0$) for level ν belonging to the lower (upper) band. The total energies in the FM (E_F) and AFM ($E_{\rm AF}$) evaluated in the thermodynamic limit of a one-dimensional chain, two-dimensional square lattice, and three-dimensional cubic lattice are shown in Figs. 5(c) and 5(d). The AFM state gives low energy throughout the parameter region of J_H and n in the three lattice types, implying that the nonequilibrium electron distribution plays a major role on the transient AFM state. This is attributable to the fact that both the difference between the band centers in the FM state and the energy gap in the AFM state are approximately $2SJ_H$ [see dotted lines in Figs. 5(a) and 5(b)].

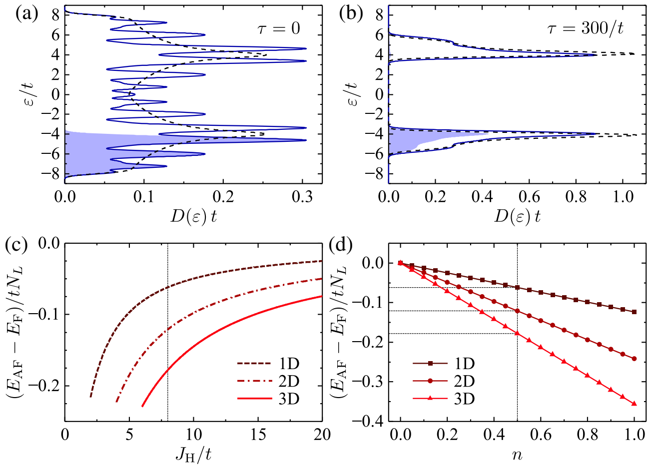

FIG. 5. (a), (b) DOS at $\tau t = 0$ (FM state), and at $\tau t = 300$ (AFM state) when the cw field is introduced. Shaded areas represent the electron distribution. Other parameter values are $A_0/t = 2$ and $\omega/t = 1$. Dotted lines represent DOS calculated from Eq. (1) where the idealized FM or AFM structures are introduced. (c),(d) Energy differences between the FM and AFM structures. We chose $n = 0.5$ in (c), and $SJ_H/t = 8$ in (d). Broken, dashed, and bold lines represent the one-dimensional chain, square lattice, and cubic lattice, respectively.

Experimental confirmations are indispensable for establishing the present proposal. Perovskite manganites $\mathrm{La}_{1-x}\mathrm{Sr}_x\mathrm{MnO}_3$ ($x \sim 0.3$) and layered manganites are the possible target materials for the metallic ferromagnets because of the DE interaction. Rather than the cw light, the use of pulse field might be realistic for the spin conversion in the present laser performance [35]. A uniform electron distribution is not required inside the wide electronic band in the initial FM state, because a dynamical cooperation between the band narrowing and FM-to-AFM conversion promotes uniform electron distribution. The observation of the AFM Bragg peak through the magnetic x-ray diffraction is a direct method for observing the transient AFM state. The disappearance of the magneto-optical Kerr signal and appearance of the two-magnon Raman scattering confirm the vanishing of the FM order and the emergence of the AFM order, respectively. The angle-resolved photoemission spectroscopy technique will be able to succeed in acquiring the expected band narrowing, electron population change, and band folding due to emergence of the AFM state.

The authors would like to thank S. Iwai, M. Naka, H. Nakao, T. Arima, and A. Fujimori for fruitful discussions. This work was supported by MEXT KAKENHI, Grants No. 26287070, No. 15H02100, and No. 17H02916. Some of the numerical calculations were performed using the facilities of the Supercomputer Center, the Institute for Solid State Physics, the University of Tokyo.

[1] A. Kirilyuk, A. V. Kimel, and T. Rasing, Rev. Mod. Phys. **82**, 2731 (2010).
[2] Y. Tokura, J. Phys. Soc. Jpn. **75**, 011001 (2006).
[3] H. Aoki, N. Tsuji, M. Eckstein, M. Kollar, T. Oka, and P. Werner, Rev. Mod. Phys. **86**, 779 (2014).
[4] E. Beaurepaire, J.-C. Merle, A. Daunois, and J.-Y. Bigot, Phys. Rev. Lett. **76**, 4250 (1996).
[5] T. Satoh, S.-J. Cho, R. Iida, T. Shimura, K. Kuroda, H. Ueda, Y. Ueda, B. A. Ivanov, F. Nori, and M. Fiebig, Phys. Rev. Lett. **105**, 077402 (2010).
[6] T. Mertelj, P. Kusar, V. V. Kabanov, L. Stojchevska, N. D. Zhigadlo, S. Katrych, Z. Bukowski, J. Karpinski, S. Weyeneth, and D. Mihailovic, Phys. Rev. B **81**, 224504 (2010).
[7] I. Razdolski, A. Alekhin, U. Martens, D. Burstel, D. Diesing, M. Munzenberg, U. Bovensiepen, and A. Melnikov, J. Phys. Condens. Matter **29**, 174002 (2017).
[8] I. Radu, K. Vahaplar, C. Stamm, T. Kachel, N. Pontius, H. A. Durr, T. A. Ostler, J. Barker, R. F. L. Evans, R. W. Chantrell, A. Tsukamoto, A. Itoh, A. Kirilyuk, T. Rasing, and A. V. Kimel, Nature (London) **472**, 205 (2011).
[9] J. H. Mentink, K. Balzer, and M. Eckstein, Nat. Commun. **6**, 6708 (2015).
[10] C. Zener, Phys. Rev. **82**, 403 (1951).
[11] P. W. Anderson and H. Hasegawa, Phys. Rev. **100**, 675 (1955).
[12] P.-G. de Gennes, Phys. Rev. **118**, 141 (1960).
[13] *Physics of Manganites*, edited by T. A. Kaplan and S. D. Mahanti (Springer, Berlin, 2002).
[14] A. Yanase, and T. Kasuya, J. Phys. Soc. Jpn. **25**, 1025 (1968).
[15] B. Bechlars, D. M. D'Alessandro, D. M. Jenkins, A. T. Iavarone, S. D. Glover, C. P. Kubiak, and J. R. Long, Nat. Chem. **2**, 362 (2010).
[16] G. Tatara, and H. Kawamura, J. Phys. Soc. Jpn. **71**, 2613 (2002).
[17] M. J. Calderon and L. Brey, Phys. Rev. B **63**, 054421 (2001).
[18] *Nanomagnetism and Spintronics*, edited by T. Shinjo (Elsevier, New York, 2014).
[19] M. Fiebig, K. Miyano, Y. Tomioka, and Y. Tokura, Science **280**, 1925 (1998).
[20] R. D. Averitt, A. I. Lobad, C. Kwon, S. A. Trugman, V. K. Thorsmolle, and A. J. Taylor, Phys. Rev. Lett. **87**, 017401 (2001).
[21] M. Rini, R. Tobey, N. Dean, J. Itatani, Y. Tomioka, Y. Tokura, R. W. Schoenlein, and A. Cavalleri, Nature (London) **449**, 72 (2007).
[22] H. Ichikawa, S. Nozawa, T. Sato, A. Tomita, K. Ichiyanagi, M. Chollet, L. Guerin, N. Dean, A. Cavalleri, S. Adachi, T. Arima, H. Sawa, Y. Ogimoto, M. Nakamura, R. Tamaki, K. Miyano, and S. Koshihara, Nat. Mater. **10**, 101 (2011).
[23] H. B. Zhao, D. Talbayev, X. Ma, Y. H. Ren, A. Venimadhav, Qi Li, and G. Lupke, Phys. Rev. Lett. **107**, 207205 (2011).
[24] H. Yada, Y. Ijiri, H. Uemura, Y. Tomioka, and H. Okamoto, Phys. Rev. Lett. **116**, 076402 (2016).
[25] S. Koshihara, A. Oiwa, M. Hirasawa, S. Katsumoto, Y. Iye, C. Urano, and H. Takagi, H. Munekata, Phys. Rev. Lett. **78**, 4617 (1997).
[26] J. Chovan, E. G. Kavousanaki, and I. E. Perakis, Phys. Rev. Lett. **96**, 057402 (2006).
[27] H. Matsueda and S. Ishihara, J. Phys. Soc. Jpn. **76**, 083703 (2007).
[28] Y. Kanamori, H. Matsueda, and S. Ishihara, Phys. Rev. Lett. **103**, 267401 (2009).
[29] W. Koshibae, N. Furukawa, and N. Nagaosa, Phys. Rev. Lett. **103**, 266402 (2009).
[30] W. Koshibae, N. Furukawa, and N. Nagaosa, Europhys. Lett. **94**, 27003 (2011).
[31] J. Ohara, Y. Kanamori, and S. Ishihara, Phys. Rev. B **88**, 085107 (2013).
[32] See, for example, S. Yunoki, J. Hu, A. L. Malvezzi, A. Moreo, N. Furukawa, and E. Dagotto, Phys. Rev. Lett. **80**, 845 (1998).
[33] An effective AFM interaction of the order of t^2/J_H is induced at $n = 1$.
[34] See Supplemental Material at http://link.aps.org/supplemental/10.1103/PhysRevLett.119.207202 for the detailed calculation method, the animation of the real-space spin dynamics, and the N_L and α dependence of the numerical results. The electron dynamics is described by the zero-temperature wave function, and a thermal effect is introduced as the random configuration of $\{\boldsymbol{S}_i\}$ in the initial state.
[35] When we chose $t = 0.5$ eV and a lattice constant $a = 5$ Å, $\boldsymbol{A}_0/t = 1(\hat{x} + \hat{y})$ corresponds to the electric field of approximately 14 MV/cm, and $\boldsymbol{A}_1 = \pi(\hat{x} + \hat{y})$ corresponds to 74 MV/cm where a 2-fs pulse width and $\omega = 1$ eV are assumed.
[36] J.-H. Park, E. Vescovo, H.-J. Kim, C. Kwon, R. Ramesh, and T. Venkatesan, Nature (London) **392**, 794 (1998).
[37] D. H. Dunlap and V. M. Kenkre, Phys. Rev. B **34**, 3625 (1986).
[38] F. Grossmann, T. Dittrich, P. Jung, and P. Hanggi, Phys. Rev. Lett. **67**, 516 (1991).
[39] T. Ishikawa, Y. Sagae, Y. Naitoh, Y. Kawakami, H. Itoh, K. Yamamoto, K. Yakushi, H. Kishida, T. Sasaki, S. Ishihara, Y. Tanaka, K. Yonemitsu, and S. Iwai, Nat. Commun. **5**, 5528 (2014).
[40] The data shown in Fig. 2 are located around $A_0/\omega = 2$ in Fig. 3(f), in which the kinetic energy is averaged between $\tau t = 400$–500. The numerical data which follow $\mathcal{J}_0(A_0/\omega)$ in Fig. 3(f) are obtained for $A_0/\omega \lesssim 1$.
[41] N. Tsuji, T. Oka, H. Aoki, and P. Werner, Phys. Rev. B **85**, 155124 (2012).
[42] N. Tsuji, T. Oka, P. Werner, and H. Aoki, Phys. Rev. Lett. **106**, 236401 (2011).
[43] J. K. Freericks, V. M. Turkowski, and V. Zlatic, Phys. Rev. Lett. **97**, 266408 (2006).
[44] M. Eckstein, T. Oka, and P. Werner, Phys. Rev. Lett. **105**, 146404 (2010).